$(2\sqrt{3} \times 2\sqrt{3})R30°$ induced self-assembly ordering by C_{60} on a Au(111) surface: X-ray diffraction structure analysis

X. Torrelles,[1] M. Pedio,[2] C. Cepek,[2] and R. Felici[3]

[1]*Instituto de Ciencia de Materiales de Barcelona, ICMAB-CSIC, 08193 Bellaterra, Barcelona, Spain*

[2]*TASC CNR-IOM TASC Laboratory, Area Science Park Building MM, SS 14, Km 163.5 Basovizza, Trieste, Italy*

[3]*ESRF, Boîte Postale 220, F-38043 Grenoble, France*

(Received 18 April 2012; revised manuscript received 25 July 2012; published 27 August 2012)

The $(2\sqrt{3} \times 2\sqrt{3})R30°$ ordering of fullerene on the herringbone reconstructed Au(111) surface has been studied using grazing incidence x-ray diffraction. The interaction between C_{60} molecules and gold atoms removes the initial herringbone reconstruction, typical of the clean Au(111) surface, and models the topmost substrate surface layer with one atom vacancy per unit cell and C-Au distances equal to 2.49 Å. The two topmost gold layers are slightly compressed. The molecule is sited on top of the vacancy and oriented with one of its hexagonal carbon rings parallel to the surface, optimizing the number of bonds between the molecule and the substrate with bond distances typical of bonds with a mixed covalent/ionic character. This configuration, that favors the formation of carbon-gold bonds, is similar to the one observed for C_{60}/Pt(111) and C_{60}/Ag(111) indicating that the adsorption of fullerenes on the (111) surface of noble metals comes with the formation of vacancies in order to minimize the system energy.

DOI: 10.1103/PhysRevB.86.075461 PACS number(s): 61.05.cp, 68.35.B−, 68.35.bd, 68.35.bp

I. INTRODUCTION

Functionalized molecular assembled films involving fullerene (C_{60}) bonded with other molecular blocks have become a very important issue in many application fields. The C_{60} interaction and reaction with surfaces is an object of intensive study, related to the development of novel artificially structured materials with controlled properties (see, for example, Ref. 1). In fact C_{60} based monolayers show unique properties and C_{60} functionalization leads to the production of tailored surface architectures on a wide variety of surfaces.[2] The study of a single C_{60} monolayer on surfaces and the processes relative to its anchoring is an essential requirement for the control of the chemical and physical properties necessary to the development of new methodologies based on incorporating C_{60} into well defined two- and three-dimensional networks.

In this context the interacting fullerenes with noble metal surfaces can be seen as a model system. Many studies are based on scanning tunneling microscopy (STM) measurements on systems ranging from isolated molecules up to ordered supramolecular assemblies.[3–9] However, scanning probe microscopy can only image the electronic density of states at the surface and provides only indirect information about the interface with the substrate. It is now largely accepted that the molecule-substrate system must be taken into account as a whole and it is not possible to simply transfer molecular functionalities, deduced from their isolated state, to the adsorbed case. A large number of experimental and theoretical works have been envisaged to single out the basic aspects governing the C_{60}-metal interaction. C_{60} forms ordered two-dimensional molecular structures on most of the low-index surfaces of metals and semiconductors. This ordering usually comes with atomic restructuring of the first atomic layers of the substrate surface and it can be used for both surface molding and surface nanopatterning.[10–16]

Previous studies of C_{60} ordered overlayer structures on Au(110) and Pt(111) surfaces[10,11,13,17] demonstrated that (i) the interface atomic arrangement is much more complex than the one inferred from STM measurements; (ii) an unexpected strong mass transport is present;[10,13] and (iii) the substrate rearranges itself to form a calyx-shaped structure where the C_{60} molecules lie.

The interest in the present paper is due to the importance of the close-packed Au(111) surface in organic-inorganic systems where it is widely used as a support for growing organic films. Moreover the three-dimensional character of C_{60} allows only few carbon atoms to be in direct contact with the substrate and is the cause for its ability to model the substrate surface. A significant number of theoretical calculations have been published providing widely spread results.[14,18–22]

In this paper we present a detailed interface structural study of C_{60} deposited on a Au(111) surface by means of surface x-ray diffraction technique (SXRD). This technique is especially well suited to the determination of complex surface reconstructions because of the weak interaction of the x rays which simplifies the theoretical description of the data (single scattering compared with the multiple scattering needed in low-energy electron diffraction). This also makes it possible to cope with large surface cell structures. Moreover, SXRD is sensitive to both the relative atomic positions within the overlayer and the adsorbate-substrate registry. However, an important limitation of SXRD for the study of molecular adsorbates is that it is only applicable to systems showing very good long-range order, as in the example of the C_{60}/Au(111)-$(2\sqrt{3} \times 2\sqrt{3})R30°$ surface reconstruction described below.

II. EXPERIMENT

The x-ray diffraction data were collected at the ID03 surface diffraction beamline of the European Synchrotron Radiation Facility, ESRF, Grenoble.[23] The x-ray beam was generated by two U35 undulators and was monochromatized with a liquid nitrogen cooled monolithic double-bounce Si(111) monochromator. Two mirrors, the first one toroidal with controllable meridional radius and the second one flat, focused

the x-ray beam at the sample position to 0.06×0.2 mm^2 (horizontal $\times$ vertical). The incident beam energy was set to 11.579 keV, lower than the Au L_{III} absorption edge to avoid the background due to the gold fluorescence. The Au(111) single crystal, surface plane parallel to the crystallographic (111) planes within 0.1° as determined by x-ray diffraction measurements, was mounted in the UHV diffraction chamber (base pressure lower than 1×10^{-10} mbar) coupled with a six-circle diffractometer and equipped with several ports for evaporators, ion sputter gun, and an Auger spectroscopy setup.[24,25] The sample temperature was controlled using a Boralectric heater (Advanced Ceramic Corp.) and monitored with a thermocouple spot welded onto one of the Ta clips holding the sample. The clean Au(111) surface exhibits the $23 \times \sqrt{3}$ herringbone reconstruction[26] corresponding to a lateral compression of the topmost surface layer of 4.4%. This compression causes the existence of parallel pairs of slightly elevated surface ridges, which separate ordered fcc and hcp domains. The Au(111)-$(23 \times \sqrt{3})$ surface was prepared by standard procedures consisting of repeated cycles of Ar^+ sputtering followed by annealing at high temperature. The process was stopped when well defined and sharp peaks corresponding to the herringbone reconstruction were observable. The Au(111) surface unit cell was described by the lattice vectors ($\mathbf{a_1}$, $\mathbf{a_2}$, $\mathbf{a_3}$) parallel to the [–110], [0–11], and [111] directions, respectively; then $\mathbf{a_1}$ and $\mathbf{a_2}$ ($a_1 = a_2 = a_0/\sqrt{2}$, the nearest-neighbor surface distance) lie in the surface plane while $\mathbf{a_3}$ ($a_3 = a_0\sqrt{3}$ with $a_0 =$ bulk lattice constant: 4.08 Å) is perpendicular to the surface. The coordinates of the corresponding reciprocal lattice vectors were denoted with H, K, L. The diffractometer was operated at a constant incidence angle of 1°.

C_{60} (purity 99.9 %) was sublimed from a tantalum crucible kept at 750 K onto the clean Au(111) herringbone reconstructed surface. The fullerene coverage was determined by Auger spectroscopy and calibrated recording the C:Au peak ratio.[10] We explored different deposition conditions as a function of Au substrate temperature, C_{60} flux, and final annealing in order to obtain a well ordered $(2\sqrt{3} \times 2\sqrt{3})R30°$ reconstruction. The quality of the obtained reconstruction was determined following the evolution of a reconstruction peak until maximum intensity and minimum width were achieved.

The highest quality $(2\sqrt{3} \times 2\sqrt{3})R30°$ reconstruction, in terms of maximum peak intensity and peak width, was obtained depositing C_{60} at low flux, about 0.05 monolayers (ML) per minute, and with a substrate temperature of 160 °C. The reconstruction fractional peaks are visible starting from a C_{60} coverage of 1/3 of a monolayer. The 1 ML $(2\sqrt{3} \times 2\sqrt{3})R30°$ reconstruction was characterized by measuring the diffracted intensities of the fractional order rods (FORs) intrinsic to this new periodicity defined by vectors ($\mathbf{a_r} = 4\mathbf{a_1} + 2\mathbf{a_2}$, $\mathbf{b_r} = -2\mathbf{a_1} + 2\mathbf{a_2}$, $\mathbf{c_r} = \mathbf{a_3}$), where ($\mathbf{a_r}$, $\mathbf{b_r}$, $\mathbf{c_r}$) are the lattice vectors of the $(2\sqrt{3} \times 2\sqrt{3})R30°$ reconstructed surface cell, and crystal truncation rods (CTRs) whose intensities contain information from both the gold substrate and the superstructure. The overall stability of the system was controlled by monitoring the intensity evolution of some reference reflections at regular intervals of time during the whole experiment.

The integrated intensities were recorded by setting the correct diffraction condition and then by rocking the crystal around its surface normal. A total of 2002 reflections, specific to the $(2\sqrt{3} \times 2\sqrt{3})$ structure were measured, which reduced to 1549 after averaging between the equivalent reflections[27] that form part of 52 FORs and seven CTRs. The (H, K, L) indices of the measured reflections defined in the basis of the Au(111) substrate were transformed to have integer (h, k) values according to base vectors ($\mathbf{a_r}$, $\mathbf{b_r}$, $\mathbf{c_r}$) of the $(2\sqrt{3} \times 2\sqrt{3})$ superstructure, i.e., (h, k, L). The standard deviations σ_{hkL} of the structure factor amplitudes $|F_{hkL}|$ were evaluated by the squared sum of a systematic error, estimated from the measurements of several equivalent reflections to be close to 9%, and of the statistical error.[28] The analysis of the symmetry-equivalent reflections shows a $p31m$ plane group symmetry for the measured data. Figure 1 shows a partial and schematic reciprocal space representation of the C_{60}/Au(111)-$(2\sqrt{3} \times 2\sqrt{3})R30°$ system. The black or color-filled circles show the distribution of reflections from the substrate or those of the $(2\sqrt{3} \times 2\sqrt{3})$ surface reconstruction, respectively.

The $p3m1$ symmetry of the Au(111) generates six equally populated C_{60}/Au(111)-$(2\sqrt{3} \times 2\sqrt{3})R30°$ domains related by a ternary axis and a mirror plane. The rotation of 30° of this superstructure with respect to the main substrate axis, i.e., $\mathbf{a_1}$, makes the symmetry of the experimental set of reflections to be $p31m$ instead of $p3m1$ as displayed in Fig. 1. Moreover, each of the six $(2\sqrt{3} \times 2\sqrt{3})R30°$ domains is able to generate the same reciprocal space pattern (Fig. 1). During the refinement

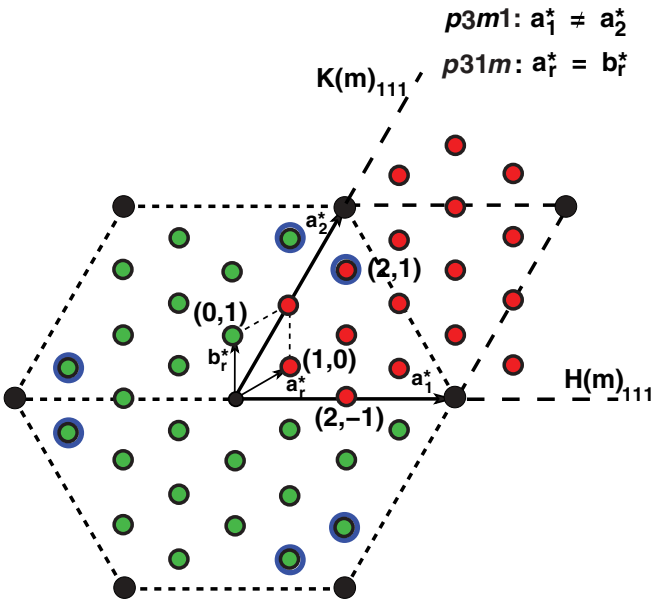

FIG. 1. (Color online) Reciprocal space diagram showing the reciprocal lattice vectors for both the Au(111) substrate ($\mathbf{a_1^*}$, $\mathbf{a_2^*}$) and the $(2\sqrt{3} \times 2\sqrt{3})R30°$ superstructure ($\mathbf{a_r^*}$, $\mathbf{b_r^*}$). The (m) label along H and K directions denotes mirror planes. (Red circles) nonequivalent portion of reciprocal space where reflections were measured; (black dots) integer order reflections; (colored dots) fractional reflections from the $(2\sqrt{3})$ superstructure. Note that ($\mathbf{a_r}$, $\mathbf{b_r}$) vectors defined in the text transform the (H,K) indices defined on the basis of the Au(111) substrate in those (h, k) of the superstructure. As an example, the equivalent reflections to (h, k) = (2, 1) are outlined in blue. The presence of six domains in the surface does not increase the number of equivalent reflections with respect to those generated by a single domain with $p31m$ symmetry.

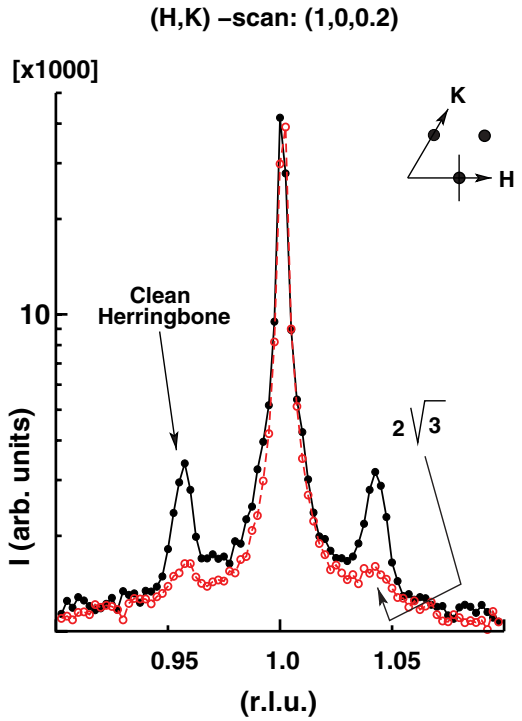

FIG. 2. (Color online) Directional scans in the reciprocal space passing through the (1, 0, 0.2) reflection. The satellite peaks in the darker line (filled black circles) correspond to the Au(111) herringbone surface structure. After C_{60} deposition and formation of the $(2\sqrt{3} \times 2\sqrt{3})R30^\circ$ the herringbone peaks have almost completely disappeared (open circles). The inset shows the scan direction for both measurements.

procedure we used six domains equally populated with $p31m$ symmetry because this symmetry is systematically broken when refining the orientation of the molecule.

III. RESULTS

Figure 2 shows two identical reciprocal space scans crossing the (1, 0, 0.2) reflection for both the clean and C_{60} covered Au(111) surfaces. The satellite fractional reflections are related to the herringbone reconstruction.[29,30] The herringbone and substrate terrace sizes were of 500 and 1000 Å, respectively, as obtained from the widths of the satellite and substrate reflections.

After C_{60} deposition at 160 °C, the intensities of the clean Au(111) herringbone reflections practically disappear indicating the release of the compressive stress of the herringbone surface reconstruction. Subsequent annealing cycles up to $T = 400\,^\circ$C did not diminish the peak widths of the C_{60}/Au(111)-$(2\sqrt{3} \times 2\sqrt{3})R30^\circ$ superstructure reflections. No sign of other fractional peaks related to other different reconstructions were detected. The dimensions of the $(2\sqrt{3} \times 2\sqrt{3})$ domains were found to be close to 1000 Å, as determined from the angular width of the $(\frac{1}{6}, \frac{1}{6}, 0.2)$ reflection, therefore similar to the substrate terrace size. Once the reconstruction was optimized in terms of the thermal treatment (i.e., no further intensity changes were observed), the sample was cooled back to room temperature and a rather extensive fractional order data set was collected in the interval of L: $0.2 \leqslant L < 4$, in reciprocal lattice units.

An ideal bulk-terminated Au(111) surface was initially used as a "guess" model to refine in a first way the site occupancies of the topmost surface atoms from the CTRs. This process demonstrated the presence of one gold atom vacancy per reconstructed surface unit cell located in the topmost surface substrate layer, as in Pt(111) or Ag(111) systems.[11,18] The new model including the C_{60} molecule on top of the vacancy is shown in Fig. 3. Figure 3(b) shows a view from down of the

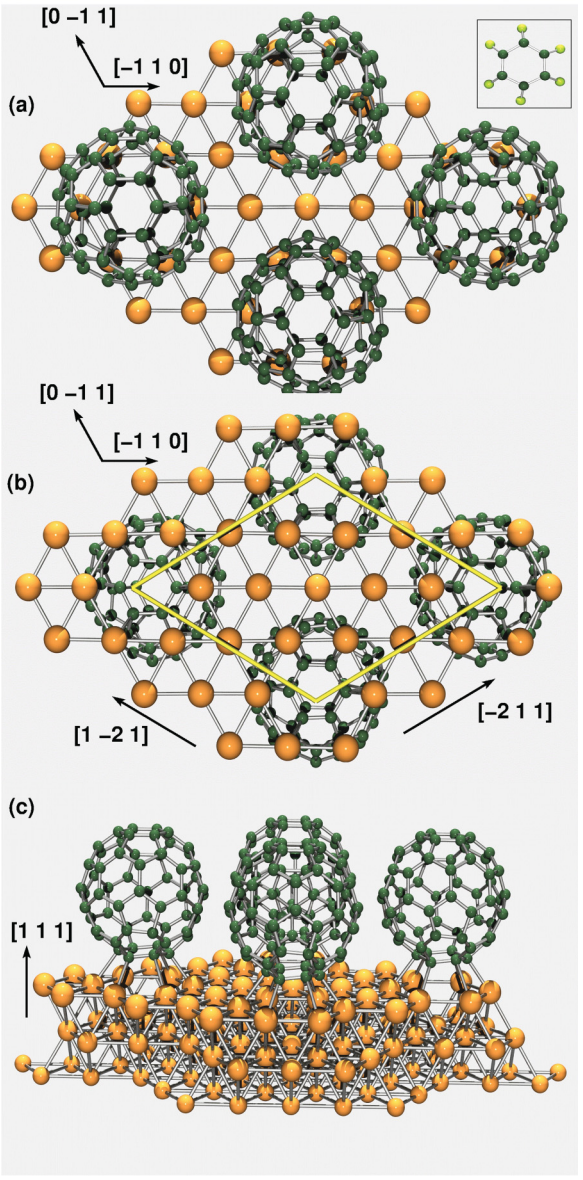

FIG. 3. (Color online) (a) Top, (b) from down, and (c) lateral views of the C_{60}/Au(111)-$(2\sqrt{3} \times 2\sqrt{3})R30^\circ$ superstructure showing the best orientation of the C_{60} molecules according to the least-squares refinement procedure. The structure corresponds to a C_{60} molecule with a hexagonal ring parallel to the substrate surface where the C atoms are aligned with the closer topmost surface Au atoms and follows the experimental $p31m$ symmetry. The rhombus line in (b) indicates the $(2\sqrt{3} \times 2\sqrt{3})R30^\circ$ unit cell. Inset: See text for more details.

$(2\sqrt{3} \times 2\sqrt{3})$ structure where only the topmost gold surface layer is shown for clarity. The corners of the unit cell (yellow) coincide with the position of the missing atoms.

To describe the full C_{60}/Au(111)-$(2\sqrt{3} \times 2\sqrt{3})R30^\circ$ reconstruction it is advantageous to fully use the symmetry operations. By considering the positions of the mirror plane and of the threefold symmetry axis located at $(\frac{2}{3}, \frac{1}{3})$, its symmetry equivalent is at $(\frac{1}{3}, \frac{2}{3})$ and the positions of all the atoms in the first layer are described by three independent gold atoms and one fullerene molecule. Applying the same methodology for the inner layer we need to refine the position of three gold atoms in the second, third, fifth, and sixth layers and four in the forth. This model with 71 gold atoms contains 41 positional (x, y, z) parameters that agree with the $p31m$ surface symmetry. The fullerene molecule is initially oriented with one of its hexagonal rings parallel to the surface and can move along the surface normal direction and freely rotate around an axis perpendicular to the surface, i.e., azimuthal rotation angle (ϕ).[31] Debye Waller (DW) parameters for each of the three topmost gold surface layers and for the C atoms of the C_{60} molecule were also included.

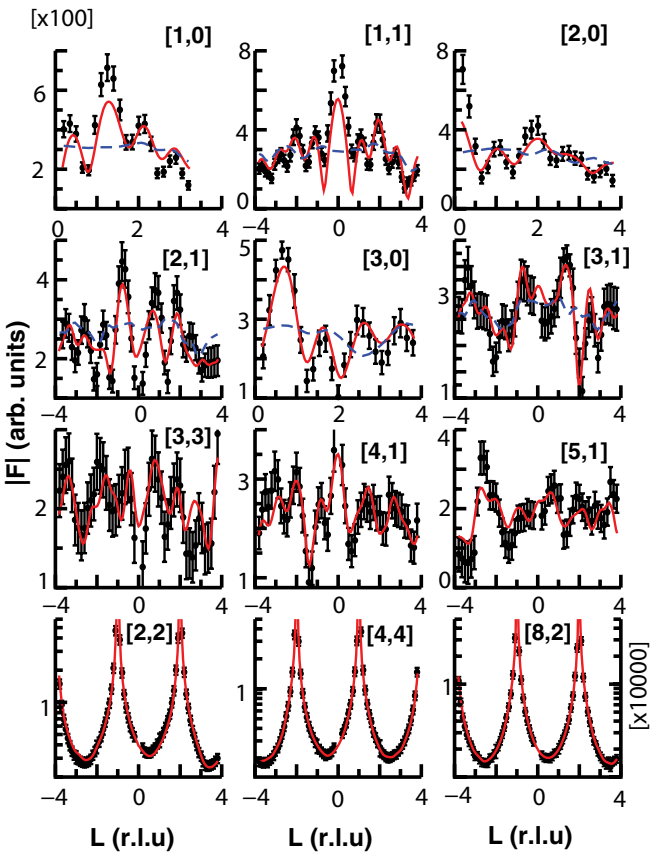

FIG. 4. (Color online) Measured structure factor amplitudes versus index L for several fractional and integer order rods. The solid red lines are the curves calculated with the best model shown in Fig. 3. The dashed blue lines were calculated removing the C_{60} molecule from the previous model. The [2, 2], [4, 4], and [8, 2] $[h, k]$ reflections correspond to the CTRs which show the typical intensity divergence close to the Bragg peak regions.

The model previously described was used to refine the total SXRD data by means of least-squares minimum procedures (LSQ). The C_{60} molecular configuration resulting from the refinement procedure shows that the C atoms of the hexagonal ring parallel to the surface are aligned and bonded to the six gold atoms distributed hexagonally around the vacancy [see Fig. 3(b)]. The χ^2 fit goodness factor of our best-fit solution is 1.3 and corresponds to the model drawn in Fig. 3, where several views are given: (a) top, (b) from down, and (c) lateral, corresponding to the final surface structure. Figure 4 shows the comparison between several fractional and integer experimental rods together with the calculated ones (red solid lines) obtained from the model drawn in the previous figure. The refined atomic coordinates of the Au atoms in the five topmost surface layers and those of the C atoms corresponding to the C_{60} molecule in the $p31m$ asymmetric unit cell are given in Table I. The columns show the bulk (x, y, z) coordinates of the Au atoms and their associated shifts from this position, expressed in lattice units, obtained from the structural refinement procedure. The uncertainties on the displacements were extracted from the least-squares analysis[27,32] and correspond to changing one parameter, with the other parameters relaxed, until χ^2 has increased by $1/(N-p)$ from its minimum value, where N is the number of nonequivalent data points, p the number of parameters in the model, and the χ^2 goodness factor is defined as

$$\chi^2 = \frac{1}{N-p} \sum_{hk} \left(\frac{|F_{hk}^{\text{calc}}|^2 - |F_{hk}^{\text{expt}}|^2}{\sigma_{hk}} \right)^2,$$

where σ_{hk} corresponds to the experimental uncertainties, and $|F_{hk}^{\text{expt}}|$ and $|F_{hk}^{\text{calc}}|$ are the experimental and calculated structure factor amplitudes from the model.

The reflection-by-reflection agreement between the observations and the calculations is also another indicator of the reliability of the model. It has become customary to describe this in terms of the residual index or unweighted residual R (Ref. 33) defined as

$$R = \frac{\sum_{hk} \left| |F_{hk}^{\text{expt}}| - |F_{hk}^{\text{calc}}| \right|}{\sum_{hk} |F_{hk}^{\text{expt}}|}.$$

The R value obtained from our best-fit solution is 9.1%, a small value that reinforces the reliability in our model.

Different molecular orientations were also explored by plotting the variation of the normalized χ^2 goodness factor versus azimuthal (ϕ: rotation around and axis parallel to $\mathbf{c_r}$) and polar angles (θ: rotation around and axis perpendicular to $\mathbf{a_r}$, i.e., an axis parallel to the y axis of the molecule in Cartesian coordinates) using as initial point the best solution showed in Fig. 3, i.e., $(\phi, \theta) = (0^\circ, 0^\circ)$. Figure 5(a) depicts the evolution of the normalized χ^2 goodness factor versus azimuth and polar angles which show sharp and well defined minima. From the χ^2 plot, three equivalent minima can be inferred for the azimuthal angle due to the presence of a threefold axis in the unit cell, while the polar angle shows two minima at $\theta = 0^\circ$ and 180°, compatible with an inversion center of the molecule. When applying a θ rotation of 360° to the molecule from

TABLE I. Atomic coordinates (in normalized lattice units, i.e., $z = z(\text{Å})/c_r$) of atoms included in the $p31m$ asymmetric unit cell for the model given in Fig. 3. The table reports the ideal bulk-terminated (x, y, z) coordinate of each gold atom with the corresponding shift $(\Delta x, \Delta y, \Delta z)$ from this position after the fitting procedure expressed in lattice units. The five topmost Au surface layers and C atoms are included. Au_{i-j} indicates Au atom j located in layer i. Only a few atoms per layer are necessary to describe the system when using the $p31m$ symmetry of the system. Gold atoms located in the outermost substrate surface layer ($i = 1$) have z coordinates close to 2 (Au_{1-j}). The average uncertainties assigned to each shift are indicated in the first line of the table. See text for more details. The coordinates and shifts of the sixth gold layer are not shown because their shifts are already included in their respective error bars.

Element	x (± 0.0005)	y (± 0.0005)	z (± 0.0005)
Au_{1-1}	1/3[a]	2/3[a]	$2.0 + 0.0067$
Au_{1-2}	$1/2 + 0.001$	0.0[a]	$2.0 + 0.0037$
Au_{1-3}	$1/6 + 0.0014$	$5/6 + 0.0008$	$2.0 - 0.0054$
Au_{2-1}	$5/6 + 0.0014$	0.0[a]	$5/3 + 0.0028$
Au_{2-2}	$1/3 + 0.0002$	0.0[a]	$5/3 - 0.0020$
Au_{2-3}	$1/6 - 0.0001$	$2/3 + 0.0001$	$5/3 - 0.0007$
Au_{3-1}	$2/3 - 0.0001$	0.0[a]	$4/3 - 0.0004$
Au_{3-2}	$1/6 - 0.0006$	0.0[a]	$4/3 + 0.0010$
Au_{3-3}	$1/6 - 0.0001$	$1/2 + 0.0006$	$4/3 + 0.0013$
Au_{4-1}	0.0[a]	0.0[a]	$1.0 + 0.0010$
Au_{4-2}	1/3[a]	2/3[a]	$1.0 + 0.0016$
Au_{4-3}	$1/2 - 0.0001$	0.0[a]	$1.0 + 0.0002$
Au_{4-4}	$1/6 + 0.0004$	$5/6 - 0.0002$	$1.0 + 0.0012$
Au_{5-1}	$5/6 - 0.0001$	0.0[a]	$2/3 + 0.0016$
Au_{5-2}	$1/3 - 0.0002$	0.0[a]	$2/3 + 0.0009$
Au_{5-3}	$1/6 - 0.0001$	$2/3 + 0.0001$	$2/3 + 0.0007$
Element	x (± 0.0030)	y (± 0.0030)	z (± 0.0020)
C	0.0714	0.1639	2.2798
C	0.1546	0.2980	2.3974
C	–0.0006	–0.2959	2.4648
C	0.0733	0.3443	2.5173
C	0.0019	–0.3420	2.6511
C	0.1276	0.3973	2.7033
C	–0.1304	–0.3991	2.7722
C	–0.0034	0.3637	2.8287
C	–0.0756	–0.3604	2.9717
C	–0.0015	0.2942	3.0144
C	–0.1313	0.1560	3.0849
C	–0.1632	–0.0895	3.2222

[a]Not refined coordinate due to symmetry constraints.

its $(\phi, \theta) = (0^\circ, 0^\circ)$ initial position, the following sequence of hexagon (H) and pentagon (P) rings is encountered: H(1):H(2):P(1):P(2):H(1′):H(2′):P(1′):P(2′) where indices (1, 1′) and (2, 2′) denote equivalent rings related by an inversion center. According to this sequence, two hexagon rings, H(1) and H(2), could be placed parallel to the surface on top of the Au vacancy. The molecular configurations when each of the hexagons are placed parallel to the surface satisfy the $p31m$ surface symmetry; however, these two configurations are not equivalent since the orientation of the whole molecule when H(1) or H(2) is parallel to the surface is different. For this reason only two minima are observed when following the evolution of the normalized χ^2 goodness factor versus polar angle in Fig. 5(a).

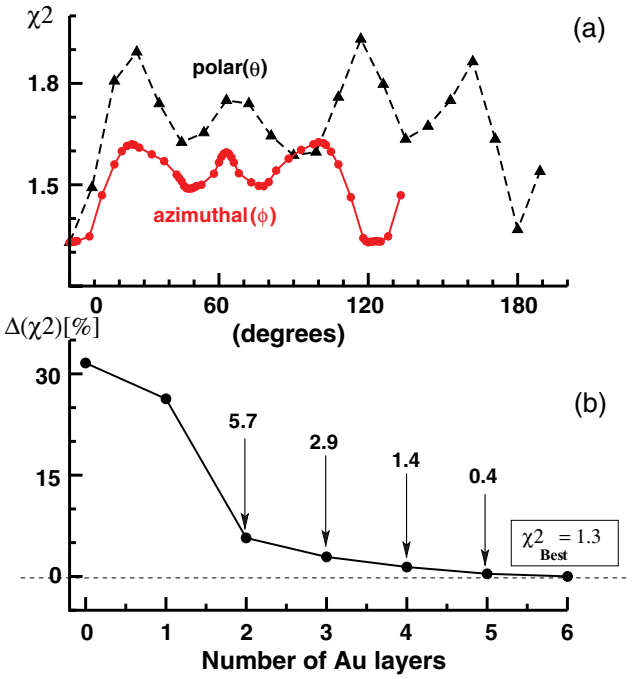

FIG. 5. (Color online) (a) χ^2 evolution versus azimuthal (ϕ) and polar (θ) angles (rotation axis defined perpendicular or parallel to the surface) from the final orientation of the molecule given by the Euler angles $(\phi, \theta) = (0^\circ, 0^\circ)$; see text for more details. The associated uncertainties for both the azimuthal and polar angles are of $\pm 1^\circ$. (b) Evolution of the increment of χ^2 in percentage from its best value ($\chi^2_{\text{best}} = 1.3$) with respect to the contribution of each gold layer included in the model during the refinement procedure. The figure helps to correctly estimate the weight of each gold layer in the data set. Considering six layers in the refinement procedure the best χ^2 is obtained, so the increment ($\Delta\chi^2$) with respect to this value is 0.0%. When the atoms of the deeper layer (layer 6) are fixed to their ideal bulk positions (this would be equivalent to removing the corresponding layer from the model) $\Delta\chi^2$ is 0.4% higher than χ^2_{best}. If layers 6 and 5 are fixed to their bulk positions the increment is 1.4%, and so on. When all layers are fixed to their ideal positions (layer 0) $\Delta\chi^2$ is ≈35% (the atomic vacancy in the topmost layer is maintained).

The uncertainties listed in Table I are expressed in lattice units as the atomic coordinates and for the gold atoms were directly obtained from the refinement procedure as indicated above. These small errors reflect the high sensitivity of the structural parameters to the data as a consequence of the high number of measured reflections (1549 nonequivalent reflections). The sensitivity of each parameter can be roughly estimated from the quantity $1/(\text{N} - p) \approx 0.0007$ ($\text{N} - p = 1549 - 48$) under the hypothesis that all the reflections are independent, which is not strictly the case in SXRD where the L dependence of the structure factor is a continuous function. Under the hypothesis that the measured reflections are independent, the uncertainty of each parameter is given by its maximum increment while the lowest χ^2 goodness factor (χ^2_{best}) remains in the range $\chi^2 < \chi^2_{\text{best}} + 0.0007$. In our case this condition holds for the uncertainties shown in Table I. The

table shows the average uncertainty corresponding to each atomic coordinate. The same condition was used to calculate the errors for the coordinates of carbon atoms. Errors in (x, y) atomic coordinates were derived from the uncertainty of the C_{60} molecule to the azimuthal rotation ($\approx\pm1^\circ$), while the error in the z coordinate was obtained from the uncertainty of the molecule with respect to its height (or interlayer C_{60}-Au spacing).

In order to evaluate the weight of the gold contribution to the experimental data, the specific contribution of each gold layer has been quantified in terms of the χ^2 goodness of fit factor. Figure 5(b) shows the evolution of χ^2 from its best value ($\chi^2_{\text{best}} = 1.3$) when the atomic positions of the six gold layers used in our model have been considered. When the atoms of the deeper layer (layer 6) are fixed to their ideal bulk positions the increment of χ^2 ($\Delta\chi^2$) is 0.4% higher than χ^2_{best}. When atoms in layers 6 and 5 are fixed to their bulk positions the increment is 1.4%, and so on. When the atoms of all layers are fixed to their ideal positions (layer 0) the increment of χ^2 is $\approx$35% (the atomic vacancy in the topmost layer is maintained). In case of an ideal gold surface termination (no gold vacancy) the χ^2 increases by $\sim$1000% due to a total absence of gold contribution to the fractional order rods. The "moderate" increase of the χ^2 shown in Fig. 5(b) is due to the small distortions of the gold layers (the CTRs seem bulklike) and to the presence of the vacancy in the topmost layer that gives a non-negligible contribution to the fractional order reflections. Once the C_{60} molecule has been placed close to the correct height with respect to the topmost gold layer (with the vacancy) the structure refinement produces a smooth evolution of the χ^2 [Fig. 5(b)] and atomic shifts with small associated errors, as would be expected from a large data set as the one measured in this experiment. The contribution of the surface gold atoms is shown for some of the fractional order rods in Fig. 4 as dashed blue lines. This contribution has been calculated from the best-fit solution removing the molecule from the model.

The C_{60} molecule is bonded to the surface through six C-Au bonds with an average bond length of 2.49 $\pm$ 0.02 Å. Note that by adding the covalent radii of C (0.77 Å) and Au (1.44 Å) the expectation value for the C-Au covalent bond length is about 2.2 Å. In the C_{60}/Au(110) model[13] the shortest C-Au bond lengths ranged between 3.1 and 3.3 Å.

The second C-Au closest distances are approximately 2.9 Å (formed between the six Au atoms surrounding the vacancy and the six nearest C atoms bonded to those of the hexagonal C ring parallel to the surface; see the lighter-color C atoms in the inset of Fig. 3). In the case of the C_{60}/Pt(111)-$(\sqrt{3}\times\sqrt{3})R13.9^\circ$ system, the C_{60} molecules formed 12 C-Pt bonds, with average bond lengths of 2.0 Å, with the six Pt atoms surrounding the vacancy. The diameter of the hole created by the Au vacancy is close to 5.8 Å, twice the nearest-neighbor Au distance and smaller than that of the C_{60} molecules (<7 Å), so the molecules cannot be embedded in the hole. The height difference between the closest C atoms of the molecule and the topmost Au-surface layer is of 1.99 Å.

The closest Au-Au distance in the bulk material is 2.88 Å, the shortest and longest in the final structure are 2.85(1) and 2.93(1) Å, respectively. The minimum value represents a bond contraction of 1% while the maximum corresponds to a length increase by 2%, close to what has already been observed in similar (111) systems such as Pt(111). The larger distortions involve atoms placed in the topmost layers that gradually decrease with surface depth. Table II shows the evolution of both the average interlayer spacing ($dz_{12}\ldots dz_{45}$) and the average intralayer buckling amplitudes ($\Delta_1\ldots\Delta_5$) obtained from the atomic z shifts of Table I and compared with those of C_{60} on Ag(111) (Ref. 18) and Pt(111) (Ref. 11) systems. The average dz_{ij} spacings and Δ_i amplitudes obtained in this work are very similar to those observed on the C_{60}/Ag(111) for the first layer. In the case of the similar C_{60}/Pt(111) system only the average interlayer distances have been determined, being very close to those of this work. In the present work the average interlayer spacing between the two topmost surface layers is compressed about 0.3%, while in silver is found an expansion of about 0.4% (Ref. 18) and 0.5% in Pt(111) (Ref. 11). The average vertical relaxations of the sixth and deeper layers are already included in their respective error bars; for this reason the atomic coordinates of the atoms in this layer are not shown in Table I, while deeper layers were not considered in the model. The sixth gold layer is the deepest surface layer giving a net contribution to the goodness of fit factor that can still be quantified, as seen in Fig. 5(b).

The distribution of atomic thermal vibration amplitudes in the refined structure was considered by assigning the same Debye-Waller thermal parameter [$\beta_C = 5.8(4)$ Å^2] to all C atoms of the fullerene molecule and one different parameter for the Au atoms of each of the three topmost surface layers: $\beta_{\text{Au}-1} = 0.95(5)$ Å^2, $\beta_{\text{Au}-2} = 0.47(5)$ Å^2, $\beta_{\text{Au}-3} = 0.35(5)$ Å^2, and $\beta_{\text{Bulk}} = 0.3$ Å^2. The rms (root mean square) vibration amplitude $\langle u\rangle$, can be easily extracted from the Debye-Waller parameter β, $\beta = 8\pi^2\langle u^2\rangle$.[34] The carbon rms vibration amplitude $\langle u_C\rangle$ is about 0.3 Å while the one of the top-layer Au atoms is about 0.05 Å. The deformation of the C_{60} molecule was also considered by adding a new parameter able to modify its volume and its shape. Deformation of the C_{60} structure was refined letting free all the structural parameters of the model. When an isotropic variation of the C_{60} volume is considered (spherical shape) the fit showed a small volume contraction (about 2 ± 0.5%) considered not relevant because of the infinitesimal improvement on the unweighted residual R factor. An elliptical type of deformation was also taken into account while maintaining constant the total volume of the C_{60} cage. In this case, no distortions from the sphericity of the molecule were detectable.

IV. DISCUSSION

As mentioned in the Introduction, the C_{60}/Au(111) system is still a scientific hot topic as evidenced by recent publications that have appeared on the subject. Different C_{60} adsorption configurations have been proposed on the basis of STM measurements[14–16] depending on the growth mode. The deposition of C_{60} molecules at RT produces a close-packed arrangement of molecules with the presence of different types of domains on the surface. The thermal annealing promotes the transformation of the different domains to the $(2\sqrt{3}\times2\sqrt{3})R30^\circ$ reconstruction. From STM and Scanning Tunneling Spectroscopy (STS) (Ref. 7) experiments at room temperature, small differences in position (and shape) of

TABLE II. Structural parameters for the relaxed C_{60}/Au(111). Dz and dz_{ij} correspond to the average C_{60}-Au and Au-Au interlayer spacing, respectively, while Δ's refer to average intralayer buckling amplitude. The numerical subscripts refer to the substrate layers. "Me" means metal type while the numerical subscripts refer to the substrate layers. The table compares these quantities with the equivalents for the Pt(111) and Ag(111) cases and those obtained from DFT calculations. The Expt/DFT column compares the experimental and calculated charge transfer from the substrate to the molecule in electron units for both systems. Table notation and definitions correspond to that of the table and figures of Ref. 18.

Me	Dz (Me-C_{60})	dz_{12}	dz_{23}	dz_{34}	dz_{45}
Au(111)	1.986(14)	2.348(10)	2.346(10)	2.353(10)	2.356(10)
Pt(111)[a]	1.4 (1.65[b])	2.277(4)	2.26	2.26	2.26
Ag(111)	2.0	2.36	2.33	2.34	2.34
DFT{Au(111)}[c]	1.80 (2.12[d])	2.32	2.34	2.35	2.35
DFT{Ag(111)}[e]	1.88	2.29	2.32	2.32	2.32
	Δ_1	Δ_2	Δ_3	Δ_4	Δ_5
Au (111)	0.019(4)	0.005(4)	0.002(4)	0.001(4)	0.001(4)
Ag(111)	0.02	0.03	0.03	0.02	0.01
DFT{Au(111)}[c]	0.04	0.09	0.01	0.01	0.01
DFT{Ag(111)}[e]	0.04	0.04	0.01	0.01	—
	Experiment/DFT (electron)	Energy vacancy formation[f]	C1s binding energy		
Au(111)	0.8[g]/0.01[h];0.2[i]	1.009	284.5[g]		
Ag(111)	1.7[j]/0.15[h];0.5[i]	1.027	284.55[k]		
Au(110)	—	0.273	284.4[l]		
Pt(111)	<0.8[m] (Expt)	1.429	284.2[k]		

[a]Values supplied by the authors of Ref. 11.
[b]Reference 41.
[c]Reference 14.
[d]Reference 20.
[e]Reference 18.
[f]Reference 39.
[g]Reference 35.
[h]Reference 19.
[i]Reference 21.
[j]Reference 38.
[k]Reference 37.
[l]Reference 36.
[m]Reference 42.

the lowest unoccupied molecular orbital (LUMO)-derived resonance, on the order of 0.1 eV, were observed for molecules adsorbed at step edges. Similar differences were also detected in regions showing a 2×2 commensurate structure of the molecular adlayer with respect to the substrate.

Density-functional theory (DFT) calculations on the C_{60}/Au(111) system[14,19–22] performed on the basis of STM experiments show that the most favored C_{60} molecular configurations occur when molecules lie on the substrate surface with a hexagonal ring parallel to it. When the model includes one atom vacancy in the topmost substrate layer the hexagonal C ring is placed on top of the vacancy;[14] on the contrary (no surface vacancy) the hexagonal C ring is located on top of hcp/fcc sites.[21] Table II shows the experimental interlayer distances for C_{60} on close Au, Ag, and Pt(111) systems that show a similar substrate local ordering induced by the interaction between the C_{60} molecule with the surface substrate. These distances are compared with those reported in the literature as results of theoretical calculations. Distances strongly depend on the atomic covalent radii and coordination number (CN), so a direct comparison of the different distances for these three systems has to be done with care. However, the direct comparison between the experimental and theoretical calculated distances for each system can be established since the coordination numbers for the different molecular configurations of the calculated models are very close to those of the experiment and can give an indication on the evolution of the theoretical interlayer distances versus the models used. In the case of the $(2\sqrt{3} \times 2\sqrt{3})R30^\circ$ reconstruction, each Au atom bonded to the C_{60} molecule has a total coordination number of 9 (8 Au-Au + 1 Au-C bond) identical to theoretical models proposing such a one-atom pit vacancy. In models where C_{60} hexagons are located on fcc/hcp sites, only three Au atoms are bonded to the molecule with a total CN of 11 (9 Au-Au + 2 Au-C bonds).[20] Finally, a horizontal comparison between the different systems can still be done in order to establish the different structural trends between them, i.e., atomic relaxation behaviors and evolution of the intralayer buckling amplitudes.

The distance between the bottom C_{60} hexagon and the top surface layer is in the 2.5–2.12 Å range on an ideal Au(111) surface termination.[20,21] This distance decreases to 2.0 Å when intermolecular van der Waals interactions are considered[22] and to 1.8 Å when a one-atom pit is included in the model.[14]

The DFT calculations for Au(111) (Ref. 14) and Ag(111) (Ref. 18) (see Table II) show systematic discrepancies for the two topmost layers on both the average interlayer spacing and the average intralayer buckling amplitude with respect to the experiment. The introduction of vacancies in the DFT models leads to a local contraction of the interlayer spacing between the two topmost layers.[14,18] However, other recent DFT calculations on C_{60} unreconstructed Au(111) surface show an expansion of 0.37% (Ref. 21), which indicates a certain dispersion on the DFT criteria.

On the other hand, spectroscopic results indicate a weaker interaction of C_{60} with the Au(111) compared to the Al(111) and Cu(111) systems and a single monolayer of C_{60} deposited on this surface shows the lowest desorption temperature, 750 K (Ref. 35), among all the metal surfaces studied so far. Photoemission and absorption experiments on the C_{60}/Au(111) system[35] conclude that the system has a metallic character and that the charge transfer is the dominant mechanism in the interface interaction. Nevertheless the broadening of the LUMO transition in Near Edge X-ray Absorption Fine Structure (NEXAFS) and the appearance of a peak in the valence band, as detected by Ultraviolet Photoelectron Spectroscopy (UPS), crossing the Fermi level and related to the long-range order formation are consistent with an anisotropic charge configuration at the interface. The photoemission C1*s* binding energy (284.5 eV) (Ref. 35) differs only slightly from the C1*s* (284.4 eV) measured for the C_{60}/Au(110)-$p(6 \times 5)$ superstructure[36] and C_{60}/Ag(111) (Ref. 37) (284.55 eV).

A recent DFT work[19] calculated the charge transfer at the interface between isolated C_{60} molecules and unreconstructed Au(111) and Ag(111) surfaces (Table II). The high discrepancy between theory and experiment[35,38] is due to model considerations: isolated molecules and unreconstructed surface substrates. C_{60} monolayers and isolated C_{60} adsorbates differ in the quality of their intermolecular as well as molecule-substrate interactions. When the same types of calculations are made on a C_{60} monolayer adsorbed on a nonreconstructed Au(111) surface,[21] the charge transfer from the substrate to the molecules is 0.2 e^-, higher than in the previous case but still far away from the experiment (Table II). This net charge transfer at the interface between the substrate and the molecule shows the ionic-covalent bond character between them, where the covalent side of these bonds can be inferred from the C_{60} molecular configuration considering that the hexagon rings have a higher number of electrons available than the pentagon rings, which would make them more efficient in forming covalent bonds.

In our previous work on C_{60}/Au(110), DFT calculations indicated that the calyx-shaped rearrangement of the substrate surface is due to the presence of directional C-Au bonds. Mass transport is facilitated on the (110) fcc surfaces of noble metals by the high mobility of atoms along the [1–10] highly packed direction and by the low energy needed for an atom to jump from one row to the next one. In the case the Au(110) surface, the number of bonds between the substrate surface atoms and the C atoms of the C_{60} molecule can be maximized by the formation of nanopits facilitated by the low energy required for the formation of surface vacancies listed in Table II.[39,40] Moreover, the large interlayer C-Au distance in this system suggests the presence of bonds with strong ionic character

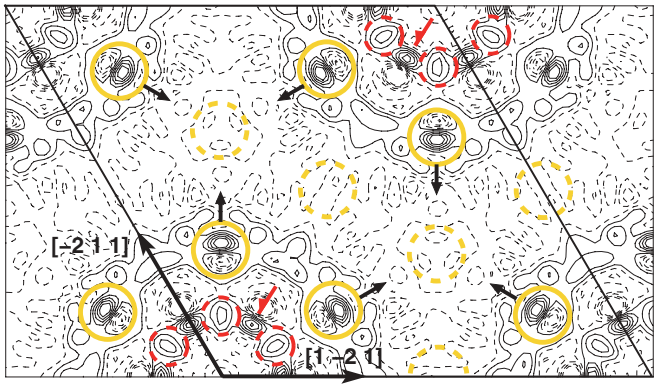

FIG. 6. (Color online) Contour map of the projected difference electronic density map calculated by subtracting the contribution of gold atoms in the topmost layer in ideal positions and removing the atom of the origin (one-atom vacancy) to the experimental electronic density obtained from the structure with atomic coordinates given in Table I. Solid-outline yellow circles correspond with the positions of the topmost gold atoms with large lateral shifts. Dashed-outline yellow circles correspond with positions of gold atoms located in special sites which show negligible (atoms on mirror planes) or absent (on threefold axis) lateral shifts. Red dashed circles correspond to the position of the C atoms bonded to the substrate. Black arrows indicate the net shift direction of the corresponding atom. Red half-arrows indicate electronic peak distribution of some carbon atoms not bonded to the substrate.

as the molecules are not fixed on the Au surface but are freely rotating. In the C_{60}/Au(111) system, and based on the C-Au distances obtained from the experiment, which are 12% larger than the covalent ones obtained from their respective covalent atomic radii, a weak ionic-covalent bond is inferred which would imply a charge transfer from the substrate to the molecule as derived from the literature.

In the C_{60}/Al(111) system, the formation of vacancies at the interface was predicted and related to a depletion of substrate charge underneath the C_{60} molecules as a consequence of the covalent character of the C-Al bonds.[43]

With the intention to visualize the effect of directional bonds on the C_{60}/Au(111) interface structure, Fig. 6 shows the projected difference electronic density map obtained by subtracting the contribution of the nondistorted topmost Au layer (where the Au atom at the origin of the unit cell is removed: one atom vacancy) to the experimental electronic density calculated using the structure given in Table I. The electronic density map has been calculated using a single domain of the $(2\sqrt{3} \times 2\sqrt{3})R30^\circ$ structure because each reflection of the diffraction pattern shown in Fig. 1 is only overlapped with equivalent reflections to it coming from each of the six domains (blue outlined circles of Fig. 1). This reciprocal space representation is equivalent to supposing that the diffraction pattern is generated by a single domain of the $(2\sqrt{3} \times 2\sqrt{3})R30^\circ$ structure with $p31m$ symmetry. A more detailed discussion is given in (Ref. 44). From this map it is possible to identify both the displacement and direction of the shift of the topmost gold atoms. The negative and positive curve levels enclosed in the yellow circles indicate that gold atoms shift away from the molecule (also indicate by the black arrow). With the subtraction of the topmost gold layer

contribution to the electronic density map we reduced the gold contribution and enhanced the weaker C contributions coming from the C_{60} molecule. In Fig. 6, yellow circles indicate the position of the Au atoms in the topmost layer while red dashed circles correspond to C atoms that are bonded to those of the substrate. It is clearly observed that C atoms bonded to Au atoms show a lower density of curve levels and are distributed on a larger region than the C atoms of the opposite hexagonal ring (some of them are indicated by red half-arrows) which are exclusively bonded to other C atoms. This behavior shows that the electronic distribution around the C atoms bonded to the substrate is lower and more disperse than in the rest of the C atoms of the C_{60} molecule confirming the partial covalent nature of the C-Au bonds.

V. CONCLUSIONS

The self-assembling structural properties of the C_{60}/Au(111)-$(2\sqrt{3} \times 2\sqrt{3})R30^\circ$ system have been studied by surface x-ray diffraction and the adsorption geometry has been determined. The final configuration of the system is based on the formation of one-atom vacancies at the gold surface where the C_{60} molecules lie with one of their hexagonal faces parallel to them similarly to the Pt and Ag cases. In this process, six C-Au equivalent bonds are formed with bond lengths of 2.49 Å while the initial herringbone reconstruction present on the clean surface disappears. The interface is stabilized via (i) vacancy formation and (ii) a partial covalent-type bonding. The molecules lie on top of the vacancies with one of the C-hexagon rings parallel to the surface. This configuration maximizes the number of electrons to form the covalent C-Au bonds. The partial ionic character of these bonds would be related to the net charge transfer from the substrate to the molecule as inferred from the literature.

The x-ray diffraction study supplied in the present work provides detailed and accurate structure information important for a better understanding of the nature of the interaction between C_{60} with noble metals as well as details on dimple formation dynamics. The reliable experimental structure values can also be used for theoretical calculations to test the accuracy of functionals and algorithms and for their development. Moreover, the accurate knowledge of molecule-substrate interactions could possibly lead to interesting applications, such as surface nanostructuring using, e.g., a regular array of adsorbed molecules. If this could be performed irreversibly the surface might be cheaply nanostructured to some desired arrangement in very precise and microscopic detail, as the formation of surface vacancies by C_{60} molecules is more general than expected since they are present on different types of metal systems with weak or stronger molecule-substrate interactions, as in Au(111) or Pt(111), respectively.

ACKNOWLEDGMENTS

This was an ESRF experiment with reference code SI-1411. X.T. thanks the Spanish MICINN Agency for partially funding this project through Grants No. CSD2007-00041 and No. MAT2009-09308. We also acknowledge the help of all the technical staff of the ID03 beamline at the ESRF and in particular T. Dufrane and H. Isern for their extraordinary support.

[1] J. Weaver and D. M. Poirier, in *Solid State Physics: Advances in Research and Applications*, edited by H. Ehrenreich and F. Spaepen (Academic Press, Boston, 1994), Vol. 48; P. Rudolf, in *Proceeding of the Xth International Winterschool on Electronic Properties of Novel Materials*, edited by H. Kuzmany, J. Fink, H. Hehring, and S. Roth (World Scientific, Singapore, 1996).

[2] D. Bonifazi, O. Enger, and F. Diederich, Chem. Soc. Rev. **36**, 390 (2007).

[3] P. Rudolf, G. Gensterblum, and R. Caudano, J. Phys. IV, Colloque **7**, 137 (1997).

[4] D. N. Futaba and S. Chiang, Jpn. J. Appl. Phys. **38**, 3809 (1999).

[5] J. K. Gimzewski, S. Modesti, and R. R. Schlittler, Phys. Rev. Lett. **72**, 1036 (1994).

[6] S. Modesti, J. K. Gimzewski, and R. R. Schlittler, Surf. Sci. **331-333**, 1129 (1995).

[7] C. Rogero, J. J. Pascual, J. Gómez-Herrero, and A. M. Barò, J. Chem. Phys. **116**, 832 (2002).

[8] T. Sakurai, X. D. Wang, T. Hashizume, V. Yurov, H. Shinohara, and H. W. Pickering, Appl. Surf. Sci. **87-88**, 405 (1995).

[9] E. Giudice, E. Magnano, S. Rusponi, C. Boragno, and U. Valbusa, Surf. Sci. **405**, L561 (1998).

[10] M. Pedio, R. Felici, X. Torrelles, P. Rudolf, M. Capozi, J. Rius, and S. Ferrer, Phys. Rev. Lett. **85**, 1040 (2000).

[11] R. Felici, M. Pedio, F. Borgatti, S. Iannotta, M. Capozi, G. Ciullo, and S. Andreas, Nat. Mater. **4**, 688 (2005).

[12] V. Langlais, X. Torrelles, Y. Gauthier, and M. De Santis, Phys. Rev. B **76**, 035433 (2007).

[13] M. Hinterstein, X. Torrelles, R. Felici, J. Rius, M. Huang, S. Fabris, H. Fuess, and M. Pedio, Phys. Rev. B **77**, 153412 (2008).

[14] L. Tang, X. Zhang, Q. Guo, Y. N. Wu, L. L. Wang, and H. P. Cheng, Phys. Rev. B **82**, 125414 (2010).

[15] L. Tang, Y. Xie, and Q. Guo, J. Chem. Phys. **135**, 114702 (2011).

[16] J. A. Gardener, G. A. D. Briggs, and M. R. Castell, Phys. Rev. B **80**, 235434 (2009).

[17] X. Torrelles, J. Rius, O. Bikondoa, P. Ordejon, E. Machado, T. L. Lee, and J. Zegenhagen, ESRF Newsletter **39**, 17 (2004)

[18] H. I. Li, K. Pussi, K. J. Hanna, L.-L. Wang, D. D. Johnson, H.-P. Cheng, H. Shin, S. Curtarolo, W. Moritz, J. A. Smerdon, R. McGrath, and R. D. Diehl, Phys. Rev. Lett. **103**, 056101 (2009).

[19] X. Lu, M. Grobis, K. H. Khoo, S. G. Louie, and M. F. Crommie, Phys. Rev. B **70**, 115418 (2004).

[20] E. Abad, J. Ortega, Y. J. Dappe, and F. Flores, Appl. Phys. A **95**, 119 (2009).

[21] L.-L. Wang and H.-P. Cheng, Phys. Rev. B **69**, 165417 (2004).

[22] I. Hamada and M. Tsukada, Phys. Rev. B **83**, 245437 (2011).

[23] O. Balmes, R. van Rijn, D. Wermeille, A. Resta, L. Petit, H. Isern, T. Dufrane, and R. Felici, Catalysis Today **145**, 220 (2009).

[24] F. Comin, R. De Martino, K. Fezzaa, V. Formoso, L. Ortega, and R. Signorato, J. Phys. IV **7**, C2/343 (1997).

[25]S. Ferrer and F. Comin, Rev. Sci. Instrum. **66**, 1674 (1995).
[26]J. V. Barth, H. Brune, G. Ertl, and R. J. Behm, Phys. Rev. B **42**, 9307 (1990).
[27]R. Feidenhans'l, Surf. Sci. Rep. **10**, 105 (1989).
[28]I. K. Robinson, *Handbook of Synchrotron Radiation* (North Holland, Amsterdam, 1991), Vol. 3.
[29]A. R. Sandy, S. G. J. Mochrie, D. M. Zehner, K. G. Huang, and D. Gibbs, Phys. Rev. B **43**, 4667 (1991).
[30]M. A. van Hove, R. J. Koestner, P. C. Stair, J. P. Biberian, L. L. Kesmodel, I. Bartos, and G. A. Somorjai, Surf. Sci. **103**, 189 (1981).
[31]X. Torrelles, E. Barrena, C. Munuera, J. Rius, S. Ferrer, and C. Ocal, Langmuir **20**, 9396 (2004).
[32]P. R. Bevington, *Data Reduction and Error Analysis for the Physical Sciences* (McGraw-Hill, New York, 1968).
[33]G. H. Stout and L. H. Jensen, *X-Ray Structure Determination* (McMillan, New York, 1968).
[34]B. E. Warren, *X-Ray Diffraction* (Addison-Wesley, Reading, MA, 1969).
[35]C.-T. Tzeng, W.-S. Lo, J.-Y. Yuh, R.-Y. Chu, and K.-D. Tsuei, Phys. Rev. B **61**, 2263 (2000).
[36]A. J. Maxwell, P. A. Brühwiler, A. Nilsson, N. Mårtensson, and P. Rudolf, Phys. Rev. B **49**, 10717 (1994).
[37]M. Pedio, K. Hevesi, N. Zema, M. Capozi, P. Perfetti, R. Gouttebaron, J.-J. Pireaux, R. Caudano, and P. Rudolf, Surf. Sci. **437**, 249 (1999).
[38]C. Cepek, M. Sancrotti, T. Geber, and J. Osterwalder, Surf. Sci. **454**, 467 (2000).
[39]P. Stoltze, J. Phys.: Condens. Matter **6**, 9495 (1994).
[40]M. Pedio, C. Cepek, and R. Felici, in *Noble Metals*, edited by Y.-H. Su (InTech, Croatia, 2012), Chap. 12.
[41]X. Q. Shi, A. B. Pang, K. L. Man, R. Q. Zhang, C. Minot, M. S. Altman, and M. A. Van Hove, Phys. Rev. B **84**, 235406 (2011).
[42]C. Cepek, A. Goldoni, and S. Modesti, Phys. Rev. B **53**, 7466 (1996).
[43]M. Stengel, A. De Vita, and A. Baldereschi, Phys. Rev. Lett. **91**, 166101 (2003).
[44]The diffraction pattern of Fig. 1 is generated by a $(2\sqrt{3} \times 2\sqrt{3})$ superstructure rotated 30° with respect to one of the main crystallographic axes of the substrate, i.e., [–1, 1, 0] (Fig. 3). Moreover, the $p3m1$ symmetry of the substrate generates six domains, i.e., three domains rotated 120° with respect to each other $\{D1(0°), D2(120°), D3(240°)\}$ plus three domains mirrored to the previous ones $\{D4(MD1), D5(MD2), D6(MD3)\}$, where (MDi) refers to the corresponding "mirrored domain i." In this case, $D4(MD1) = D3(240°)$, $D5(\mathrm{MD2}) = D2(120°)$, and $D6(MD3) = D1(0°)$. On the other side, the equivalent reflections of a $p31m$ diffraction pattern generated from a single domain are related by the symmetry operations $R(0°) = (h, k)$, $R(120°) = (-h-k, h)$, $R(240°) = (k, -h-k)$, $M(1) = (k, h)$, $M(2) = (-h-k, k)$, $M(3) = (h, -h-k)$, where R and M refer to rotation or mirror plane operation symmetries, respectively; consequently the intensity contribution to each reflection of the diffraction pattern coming from one single domain would be $I_{hk}(1) \approx \sum_{(R1\mathrm{to}3, M1\mathrm{to}3)} |F_{hk}|^2 \approx j|F_{hk}|^2$ where j would be the number of equivalent reflections to a given one (multiplicity). When considering six equally populated domains as those described above, the intensity contribution to each reflection would be $I_{hk}(6) \approx \sum_{(D1\mathrm{to}6)} \sum_{(R1\mathrm{to}3, M1\mathrm{to}3)} |F_{hk}|^2 \approx j|F_{hk}|^2$. Since $I_{hk}(1) = I_{hk}(6)$, the electronic density map of Fig. 6 can be generated considering exclusively one single domain with $p31m$ symmetry.